NATIONAL ADVISORY COMMITTEE FOR AERONAUTICS

TECHNICAL NOTE

No. 1189

PRESSURE-DISTRIBUTION MEASUREMENTS ON THE ROTATING BLADES OF A SINGLE-STAGE AXIAL-FLOW COMPRESSOR

By Jack F. Runckel and Richard S. Davey

Langley Memorial Aeronautical Laboratory
Langley Field, Va.

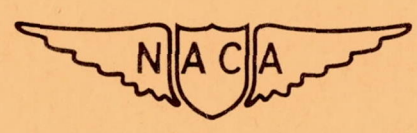

Washington
February 1947

NATIONAL ADVISORY COMMITTEE FOR AERONAUTICS

TECHNICAL NOTE NO. 1189

PRESSURE-DISTRIBUTION MEASUREMENTS ON THE ROTATING BLADES OF A SINGLE-STAGE AXIAL-FLOW COMPRESSOR

By Jack F. Runckel and Richard S. Davey

SUMMARY

A preliminary investigation has been made of the pressure distribution about the mean-radius section of the rotating blades of a single-stage axial-flow compressor at a blade Mach number of 0.35. A 24-cell pressure-transfer device used in obtaining the pressure data is described and the accuracy of these data is established by several independent methods.

The results obtained indicated that the maximum suction pressure for the thin low-camber rotor blades tested (stagger, 70°, and solidity, 0.86, at mean-radius section) was only slightly greater than for the isolated airfoil of the same section. The lift-curve slope for the rotor blades was much lower than that estimated from theoretical calculations for a comparable two-dimensional cascade, indicating the necessity of using cascade test data to determine the blade-angle settings. Stalling of the flow in the compressor was found to originate at the root and tip sections of the blade owing to the effects of casing boundary layers, improper blade twist, and large clearances.

INTRODUCTION

Improvement in the performance of axial-flow compressors requires information concerning the details of the flow around the blades. Because of the difficulty of making measurements on rotating blades, past research on blade performance has been restricted mainly to investigations of the flow about stationary two-dimensional cascades of airfoils. These studies (references 1 and 2) have yielded valuable information on the fundamentals of airfoil performance as affected by the geometry of the cascade. Experimental airfoil data obtained in cascade have been used successfully in the design of blading for low-speed blowers in which the pressure rise produced and the operating condition for best efficiency agreed with predictions based

on the cascade test data. At high Mach numbers, however, it is not known whether the three-dimensional and centrifugal effects present in rotating machines but not present in stationary cascades will invalidate the use of cascade test data. It is considered that these effects may also be of importance at low Mach numbers in the region of blade stall. An investigation of blade pressure-distribution characteristics for a single-stage axial-flow compressor has been started, therefore, at the Langley Memorial Aeronautical Laboratory with the object of securing blade performance data under actual operating conditions.

A pressure-transfer device capable of simultaneously transferring 24 pressures from a rotating blade to a stationary multitube manometer has been developed for this project. The present preliminary report briefly describes the pressure-transfer device, the tests to establish its accuracy, and its first application in an investigation of the blade flow characteristics of a compressor having thin low-camber blades of NACA 16-series propeller sections.

A particular objective of the compressor tests was to determine the nature of the blade stall, which appeared to be occurring prematurely. The tests were made at a moderate Mach number of about 0.35.

SYMBOLS

a local velocity of sound in air, feet per second

c chord of compressor blade, feet

c_l section lift coefficient

c_n section normal-force coefficient

C_P total-pressure-rise coefficient $\left(\frac{\Delta P_{1-3}}{\rho_1 n^2 D^2}\right)$

c_p specific heat at constant pressure, foot-pounds per slug per $^{\circ}F$

C_T torque coefficient $\left(\frac{\text{Net torque}}{\rho_1 n^2 D^5}\right)$

(Net torque = Shaft torque − Measured tare without blades;
Tare = Windage on rotor disk + Torque absorbed by pressure-transfer device)

D	tip diameter, feet
g	acceleration of gravity, feet per second per second
M	Mach number $\left(\frac{V_m}{a}\right)$
m	mass flow, slugs per second
n	rotational speed of rotor, revolutions per second
P	absolute total pressure, pounds per square foot
p	absolute static pressure, pounds per square foot
p_a	atmospheric pressure, pounds per square foot
Q	volume rate of flow, cubic feet per second
q	dynamic pressure, pounds per square foot $\left(\frac{1}{2}\rho V^2\right)$
R	gas constant for air, Btu per pound per $^{\circ}F$
R_N	Reynolds number $\left(\frac{\rho V_m c}{\mu}\right)$
r	radius, feet
T	absolute temperature, $^{\circ}F$ absolute
U	rotor speed, feet per second
V	air velocity relative to casing, feet per second
W	air velocity relative to rotor blade, feet per second
w	whirl velocity, feet per second
x	chordwise distance from leading edge, feet
$\frac{mg\sqrt{\theta}}{\delta}$	equivalent weight flow, pounds per second
α	section angle of attack, degrees
β	stagger angle, degrees
γ	ratio of specific heats

δ ratio of inlet-air total pressure to NACA standard sea-level pressure $\left(P_1/p_o\right)$

η efficiency where total pressures are weighted averages from surveys across annulus $\left(\frac{mc_pT_1\left[\left(\frac{P_3}{P_1}\right)^{\frac{\gamma-1}{\gamma}}-1\right]}{2\pi n(\text{Net torque})}\right)$

θ ratio of inlet total air temperature to NACA standard sea-level temperature $\left(T_1/T_o\right)$

μ viscosity of air, pound-seconds per square foot

ρ mass density, slugs per second

σ solidity (blade chord divided by gap between blades)

ϕ turning angle relative to rotor blade, degrees

Subscripts:

o sea level

1 inlet measuring station ahead of stator

2 measuring station between stator and rotor

3 outlet measuring station behind rotor

ax axial direction

ℓ orifice on blade surface

m mean based on average of entering and leaving air vectors (see fig. 4)

APPARATUS

General arrangement.- A diagram of the test setup is shown in figure 1. The 42-inch compressor was driven by a 1000-horsepower electric motor mounted on bearings to permit torque measurements. The air from the compressor was decelerated in an 8° conical diffuser, straightened in honeycomb vanes, and then accelerated in a 30-inch

venturi which permitted accurate determination of the weight flow. A second diffuser downstream from the venturi made it possible for the compressor to pump larger weight flows of air than could be produced without the diffuser-venturi system. Back pressure (and hence weight flow for a given compressor speed and geometry) was controlled by means of an adjustable plug at the outlet of the system.

Compressor.- A sketch and a photograph of the compressor are shown in figures 2 and 3. The compressor consisted of 37 stator blades located 6 inches ahead of 24 rotor blades. The diameter of the inner casing was 29 inches and that of the outer casing was 42 inches, making the root-tip ratio 0.68. Figure 2 indicates the manner in which the pressure tubing from one of the rotor blades was led through a channel inside the rotor disk to the axis of the rotor and thence to the pressure-transfer device. Although operated only at 1800 and 2100 revolutions per minute in the present tests, the compressor is capable of a maximum speed of about 4000 revolutions per minute. The compressor has recently been adapted for blade research; it was originally designed and used for other purposes. The original low-camber blading of the compressor, which was known to be of poor aerodynamic design, was used in the present exploratory tests.

A typical velocity diagram for the mean-radius section of the rotor blade is shown in figure 4. It is seen that the stators turn the air against the rotor. Values for the velocities and angles of figure 4 are given in table I for three operating conditions (A, B, and C). The root and tip sections referred to in table I are taken 1 inch from the casings. The stator blades produced approximately a vortex distribution of tangential velocity. The rotor blades, however, produced lower axial velocities near the root than the outer half of the blades.

Rotor blades.- A photograph of the rotor blades mounted in the rotor is shown in figure 3, and a sketch giving additional details is shown in figure 5. The blades had a span of about 6.50 inches and a constant chord of 4 inches giving an aspect ratio of 1.625. The blade-angle setting at the hub section was 25.4° measured from the plane of rotation and the blade twist was 4.3°, making the tip angle 21.1°. The solidity at the mean-radius section was 0.86. The blade-section profiles varied from the NACA 16-(6)(09) at the root to the NACA 16-(4.5)(06) at the tip. The mean-radius section was the NACA 16-(5.3)(07.6). Ordinates for these sections were obtained by the method of reference 3. At the time the blades were designed no cascade-developed sections of low camber were available. Tip clearance

of the rotor blades averaged about 0.040 inch. One rotor blade had 24 surface pressure orifices at its mean section. (See fig. 5.)

Stator blades. The stator blades were designed with a mean line having the desired turning angle, which was obtained from reference 4, and an NACA 0009-64 section (reference 5) was superimposed on this mean line. The solidity at the mean-radius section was 1.328. These blades had the same span and chord, 6.5 inches and 4 inches, respectively, as the rotor blades. The blade-angle setting measured from the compressor axis was 27.7° at the hub section. The twist was 8.1°, making the tip angle 19.6°. One stator blade had 24 surface pressure orifices at its mean-radius section, which were located in the same relative chordwise positions as those on the rotor blade.

Pressure-transfer device.- The pressure-transfer device, developed for measuring pressures on rotating propeller and compressor blades, employs rotating mercury to provide the necessary seal between the rotating and stationary parts. The device consists of a rotating hollow shaft with a series of integral impeller disks rotating between fixed annular disks that form part of the casing. The impeller diameter is 3 inches and the over-all length of the device is 18 inches.

A photograph of the pressure-transfer device with the top of the casing removed to show the impellers and fixed disks is presented in figure 6. Each cell formed by a fixed disk and two impellers had a small rotating pressure orifice entering into it from the rotating hollow shaft and a fixed orifice leading out through the stationary disk. A schematic sketch of a single cell is shown in figure 7. The impeller causes the mercury to rotate and form an annular seal around the periphery of the impeller, thus forming a seal between adjacent cells. The mercury seal was capable of transferring a pressure difference of about one atmosphere without leaks at 2100 revolutions per minute, the speed of the present tests. The pressure differences that the transfer device is capable of transmitting are proportional to the square of the rotational speed. The performance of the transfer device has been investigated in bench tests and found satisfactory from 500 to 6000 revolutions per minute. A water jacket is provided for cooling at speeds above 2000 revolutions per minute. The device now in use has 24 cells, thus permitting the simultaneous transmission of 24 pressures.

The cells of the transfer device can be checked for leaks during the course of a series of blade tests by sealing the blade orifices and applying pressure from the manometer side.

Instrumentation.- The pressures obtained through the use of the pressure-transfer device were corrected for the effect of centrifugal force acting on the air column in the connecting tubing between the orifice and the pressure-transfer device. As this correction involves the temperature of the air column, a calibrated Baldwin-Southwark temperature gage was installed inside the rotor at the mean rotor radius. The temperature was obtained by measuring the resistance across the gage. Three slip rings were used to transmit the potential from the gage in the rotor to a Wheatstone bridge.

Static-pressure orifices were located in the inner and outer casing at the survey stations. Values of total pressure, static pressure, and stream angle were determined by the use of survey apparatus consisting of total-pressure, static-pressure, and yaw tubes in the same radial plane. The survey apparatus was adjustable in radial position so that a complete survey across the annulus could be made during a test run. The survey tube at station 2 was also adjustable tangentially. Survey instruments at stations 1 and 3 were mounted on one side of the casing and at station 2 on the opposite side.

REDUCTION OF DATA

The testing procedure consisted of varying the air-flow quantity to obtain a range of lift coefficients and angles of attack for the test airfoil. All tests were run at a constant speed of 2100 revolutions per minute except one which was run at 1800 revolutions per minute. Airfoil surface pressures were transmitted by the pressure-transfer device to a multitube manometer and photographed. These pressures were corrected for centrifugal effect by means of the following equation:

$$p_l = p' e^{\frac{2\pi^2 n^2}{gRT}\left(r'^2 - r_s^2\right)}$$

where

p_l true local absolute static pressure at blade orifice, pounds per square foot

p' uncorrected absolute static pressure at manometer, pounds per square foot

r' radius to orifices in test blade, feet

r_s radius to orifice in rotating shaft of pressure-transfer device, feet

$\overline{T}$ absolute mean temperature of air in rotor tubing, °F absolute

The average value of this correction was about 5 percent of the absolute pressure.

Nondimensional pressure-distribution diagrams for isolated airfoils are ordinarily based on the dynamic and static pressures of the free stream. The static pressure ahead of and behind the airfoil is the same, and so are the free-stream velocities and direction of flow. In the compressor, however, there was a static-pressure drop and an increase in air velocity across the stator blades and a static-pressure rise and a decrease in velocity across the rotor blades with corresponding changes in flow direction. A mean air condition was therefore selected as a basis for defining the pressure coefficients and angles of attack. This mean air condition is designated by the subscript m and is shown on the vector diagram of figure 4. The rotor-blade pressure coefficients used in this report are defined as

$$\frac{p_l - p_m}{q_m}$$

where

p_m average static pressure between stations 2 and 3 at rotor-blade semispan $\left(\frac{p_2 + p_3}{2}\right)$

$q_m = \frac{1}{2}\rho_m V_m^2$

$\rho_m = \frac{\rho_2 + \rho_3}{2}$

V_m mean air velocity (see fig. 4)

Pressure distributions based on similar definitions of the mean air were used in the case of the stator blade.

Section normal-force coefficients were obtained by integrating the pressure distribution around the airfoil

$$c_n = \oint_0^{1.0} \frac{p_l - p_m}{q_m} \frac{dx}{c}$$

and the lift coefficient was computed from

$$c_l = c_n \cos \alpha$$

with the drag neglected.

A study of the possible sources of inaccuracy for the quantities measured in these tests indicated that the angles obtained by use of the survey apparatus are probably correct to within $\frac{1^\circ}{2}$. There are believed to be no significant errors in any of the other measurements.

RESULTS AND DISCUSSION

Performance of Compressor

The torque, the pressure rise, and the efficiency characteristics of the compressor are shown in figure 8 as functions of the equivalent weight flow. The conditions A, B, and C noted on the figure represent operating conditions for which analysis is to be made and for which detailed data are shown in tables I and II. At condition B the blades operate close to peak efficiency. For condition A the weight flow was reduced until the compressor started to surge and a reduction in outlet pressure started to occur. This condition of operation resulted in some vibration; however, the vibration was not so violent that the machine could not be operated continuously. One of the objectives of these tests was to investigate the nature of the incipient blade stall at condition A, because the stall was occurring sooner (that is, at a higher weight flow and lower outlet pressure) than was expected from calculations based on isolated-airfoil maximum-lift data. Condition C was a high-weight-flow low-pressure-rise condition.

Performance of Pressure-Transfer Device

As mentioned previously, the pressures indicated by the pressure-transfer device include the centrifugal pressure of the rotating column of air in the tube leading from the orifice on the blade inward to the rotor of the transfer device. This centrifugal pressure is an

appreciable fraction of the incremental pressures on the rotating blade and must therefore be determined accurately. All the quantities in the equation previously given for computing the centrifugal effect can be determined with a high order of accuracy. The only quantity that is difficult to measure is the mean temperature of the air in the rotor tubing. In order to establish the accuracy with which the centrifugal factor was determined, pressure distributions were obtained for the same blade angle of attack at two different speeds, 1800 and 2100 revolutions per minute. The Mach number change (0.30 to 0.35) for this change in speed was so small as to cause no appreciable change in the nondimensional pressure distribution. The results of this comparison are shown in figure 9. It is shown that the pressure diagrams for the two speeds are identical in spite of a large change in the centrifugal factor which increased for a typical tube from 86.1 to 118.6 pounds per square foot in going from 1800 to 2100 revolutions per minute. The mean dynamic pressures were 134.7 and 183.4 pounds per square foot, respectively, for 1800 and 2100 revolutions per minute. The coincidence of the diagrams of figure 9 indicates that the factor was accurately accounted for.

As further check on the accuracy of the pressure data, the lift coefficients obtained from integrations of the pressure diagrams were compared with lift coefficients calculated from the theoretical two-dimensional relation between the lift, the pressure rise through the rotor, and the change of tangential velocity produced by the rotor. This relation (from reference 1) is

$$c_l = \frac{1}{\sigma}\sqrt{\left(\frac{\Delta p}{q_m}\right)^2 + \left(\frac{2\Delta w \bar{V}_{ax}}{W_m^2}\right)^2}$$

in which $\bar{V}_{ax}$ is the mean of the entering and leaving axial-velocity components. All the quantities under the radical in this equation were measured in the surveys made at stations 2 and 3. It should be pointed out that the lift coefficient determined by this relation was subject in the present tests to possible error of about ±0.04 due primarily to small errors in the measurement of the flow angles. Thus only an approximate agreement with the pressure-distribution data would be expected. The lift-coefficient comparison is as follows:

Condition	Lift coefficient	
	From integrated pressure distributions	Calculated from flow surveys
B	0.55	0.58
C	.44	.44

Within the limit of accuracy of the flow-survey data this comparison satisfactorily establishes the accuracy of the pressure-distribution data obtained with the pressure-transfer device.

A further test of the accuracy of the pressure-transfer device has been made in another installation in which the pressure indicated by a rotating total-pressure tube was found to be equal to the calculated total pressure.

Pressure Distribution

Figure 10 presents rotor-blade pressure-coefficient diagrams for mean angles of attack ranging from 0.7° to 6.3°. The consistency and small scatter of the data are indicative of the precision of measurement and the satisfactory performance of the pressure-transfer device. The diagram for $\alpha_m = 3.0^\circ$, $c_l = 0.55$ shows the flat pressure distribution characteristic of the NACA 16-series airfoil section when operating near its design lift coefficient (0.53 in this case). At angles of attack less than 3.0° suction pressure peaks develop on the lower surface near the leading edge and at higher angles similar peaks occur on the upper surface of the blade.

When the angle of attack was increased from 4.3° to 6.3°, the lift coefficient was found to decrease from 0.65 to 0.54. At first glance it would appear that stalling of the section had occurred. Closer inspection of the diagram for $\alpha_m = 6.3^\circ$, however, shows a high degree of pressure recovery on the upper surface near the trailing edge. If the section were stalled, the pressures for some distance ahead of the trailing edge would be equal. As will be discussed in more detail later, this loss in lift at the mean section was found to be associated with stalling of adjacent sections of the blade near the root and tip.

Pressure diagrams for the stator blade are shown in figure 11. The peak negative pressure coefficient and the lift coefficient for the stator are larger than for the rotor as shown by comparing the lower part of figure 11 with figure 9. The actual peak suction pressures on the stator, however, are lower than on the rotor as indicated in the top part of figure 11; the speed of sound and compressibility difficulties would thus occur first on the rotor if the speed of the rotor were increased.

The diagrams shown in figure 10 for conditions B and C (see fig. 8) have been enlarged and compared in figure 12 with calculated theoretical diagrams for the NACA 16-(5.3)(07.6) airfoil section operating as a two-dimensional isolated airfoil at the same lift

coefficient. The method of reference 6 was used in calculating the theoretical diagrams. Unfortunately, no stationary cascade data, either experimental or theoretical, were available for comparison with the present test results. The calculated pressure distribution for the isolated airfoil on the suction side is surprisingly similar to the rotor-blade data for conditions B and C. (See fig. 12.) It might be expected, of course, that the pressure coefficients ahead of the 50 percent station of the test blade would be more negative and those behind the 50 percent station would be more positive than those in the isolated case because of the pressure rise across the rotor blades. The data of figure 12 clearly show this effect on the suction side of the blades.

The positive pressure side of the blade has pressure distributions for conditions B and C similar in form to those of the isolated airfoil, but the measured pressures are generally more positive in value. (See fig. 12.)

A principal point of difference between the isolated-airfoil diagrams for conditions B and C and the test results exists in the lift distribution as determined from the difference between the upper and lower surface pressures. The rotor blades tend to be more highly loaded over the forward part of the blade. Toward the rear of the blade the loading becomes considerably lower than is indicated by the calculation for the isolated airfoil although some decrease in loading over the rear portion of an isolated airfoil is indicated from wind-tunnel tests. A similar effect was noted in the stationary cascade tests of reference 2. This effect can be explained by reference to the velocity diagram (fig. 4) which shows that the forward part of the blade is subject to a higher velocity W_2. It appears that a more desirable loading might be achieved through use of a camber line having more curvature near the rear of the blade.

Critical Mach Number

Figure 12(b), which shows the pressure diagram for the peak-efficiency condition, indicates a slightly higher suction pressure on the upper surface of the rotor blade than does the theoretical diagram for the isolated airfoil. It would thus be expected that the critical Mach number for the rotor blades would be somewhat less than predicted from isolated-airfoil data. If it is assumed that the rate of increase in suction pressure with Mach number is the same for the rotor blades as for the isolated airfoil, the critical Mach number estimated by the method of von Karman and Tsien is found to be 0.69 as compared with 0.72 for the isolated airfoil. It appears that the critical Mach number of the rotor blade could be increased by

increasing the camber toward the rear of the blade and thereby producing a more uniform loading.

Lift Characteristics

The lift coefficients obtained from integration of the pressure diagrams are plotted against angle of attack in figure 13 and are compared with lift data obtained in tests of the isolated airfoil in the Langley 24-inch high-speed tunnel (reference 3.) The tunnel tests were run at a Mach number of 0.3 and a Reynolds number of 700,000, conditions closely approaching those of the rotor-blade tests in which the Mach number varied from 0.3 to 0.41 and the Reynolds number varied from 774,000 to 929,000. Tunnel test data for the NACA 16-(5)(06) and 16-(5)(09) airfoil sections were interpolated to obtain the result shown in figure 13 for the NACA 16-(5.3)(07.6) airfoil section. The theoretical lift curve for the isolated airfoil is also shown.

Results of lift-curve-slope calculations for cascades of thin flat plates given in reference 1 indicate that the theoretical lift-curve slope for the stagger and solidity of the present tests is considerably greater than that of the isolated airfoil. The theoretical lift curve for the flat-plate cascade is shown in figure 13. Because of the low camber and thinness of the test blades, it is considered that the theoretical lift-curve slope for the flat-plate cascade may be used as a rough approximation for the test blades. Figure 13 shows that the lift-curve slope is lower for the rotor-blade test than for the isolated airfoil, and much lower than the theoretical slope for the flat-plate cascade. It is evident that neither the isolated-airfoil data nor the theoretical cascade calculations can be used to predict rotor-blade angle settings and therefore cascade test data must be used.

The maximum lift coefficient occurring at the mean-diameter section is shown in figure 13 to be 0.68. The stalling lift coefficient for the isolated airfoil was about 1.06. It was first thought that the rotor blade section stalled at a lift coefficient of 0.68. Study of the pressure diagrams (fig. 10), however, shows clearly that the flow is unstalled since pressure recovery on the upper surface extends all the way to the trailing edge. It became apparent therefore that a stall must be occurring either at the root or tip section in order to account for the surging of the compressor and the decrease in over-all total-pressure rise for condition A. In order to investigate this possibility, the lift coefficients for root and tip sections located 1 inch from the inner and outer casings were computed from the survey measurements of flow angles and velocities by the relation given previously. The results obtained are shown in the following table:

	Root section	Mean section	Tip section
Condition C			
α_m, deg	2.2	1.6	0.5
c_l	0.53	0.44	0.43
Condition B			
α_m, deg	4.5	3.0	2.1
c_l	0.74	0.55	0.53
c_l (design camber)	0.58	0.53	0.47
Condition A			
α_m, deg	12.1 } Stalled	6.3	4.5 } Stalled
c_l	0.10 }	0.54	0.14 }

For the low angle of attack condition C and the peak efficiency condition B the mean and the tip sections operate at about the same lift coefficients while the root section operates at a considerably larger lift coefficient. For condition B the lift coefficient for the mean section was only slightly greater than the lift coefficient for which the section was cambered (0.53). The root and tip sections, however, operated at lift coefficients considerably higher than the values for which these sections were cambered (0.58 and 0.47, respectively). When the weight flow was decreased to that of condition A, the surge condition, the table shows that the root section became badly stalled, developing a lift coefficient of only 0.10 at an angle of attack of 12.1°. A less severe stall occurred at the tip section where the lift coefficient dropped to 0.14 at an angle of attack of 4.5°. These root- and tip-section values for condition A must be considered only qualitative because of the impossibility of accurate flow-angle measurements in stalled flow. These large losses in lift at root and tip caused a reduction in lift for the entire blade with the result that the lift of the mean section is reduced. As previously explained, the root and tip stalls do not extend to the mean section for operating condition A, this fact being clearly shown by the pressure diagram for $\alpha_m = 6.3°$. (See fig. 10.)

The primary cause of the stalls occurring at the root and tip is considered to be the excessive loadings of the root and tip sections in the presence of casing boundary layers which were about 3/4 inch thick at the entrance to the rotor. Contributing factors were the large clearances (1/8 inch) at the rotor-blade root and the poor aerodynamic shape of the blade tips. (See fig. 5.) It is also apparent that the root section in particular was considerably under-cambered for the flow conditions which existed. Reference to the preceding table shows that the blade twist was not correct in that the lift-coefficient distribution along the blade (for condition C or B) did not conform to the distribution for which the blade was cambered. It is apparent that this improper twist aggravated the stalling of the blade root and tip sections and hence reduced the range of operation of the compressor.

CONCLUDING REMARKS

A preliminary investigation has been described in which a newly developed 24-cell pressure-transfer device was used to determine the pressure distribution about the mean-radius section of a rotating blade in a single-stage axial-flow compressor operating at a blade Mach number of 0.35. The fact that the pressures on the rotating blade were correctly indicated by the pressure-transfer device was verified by several independent methods.

The pressure data showed that the maximum suction pressures for the rotor blades were only slightly greater than for the isolated airfoil of the same section. The lift-curve slope for the thin low-camber blades tested was much lower than the theoretical slope of a comparable two-dimensional cascade of flat plates, indicating that cascade test data must be relied on to determine blade settings. At the surge point of the compressor the blades were found to be stalled at the root and tip sections but the flow at the mean section was not stalled. The presence of casing boundary layers, improper blade twist, and large clearances contributed to the stalling of the root and tip sections.

Langley Memorial Aeronautical Laboratory
National Advisory Committee for Aeronautics
Langley Field, Va., September 11, 1946

REFERENCES

1. Weinig, F.: Die Strömung um die Schaufeln von Turbomaschinen. Johann Ambrosius Barth (Leipzig), 1935.

2. Bogdonoff, Seymour M., and Bogdonoff, Harriet E.: Blade Design Data for Axial-Flow Fans and Compressors. NACA ACR No. L5F07a, 1945.

3. Stack, John: Tests of Airfoils Designed to Delay the Compressibility Burble. NACA TN No. 976, Dec. 1944. (Reprint of ACR, June 1939.)

4. Patterson, G. N.: Note on the Design of Corners in Duct Systems. R. & M. No. 1773, British A.R.C., 1937.

5. Stack, John and von Doenhoff, Albert E.: Tests of 16 Related Airfoils at High Speeds. NACA Rep. No. 492, 1934.

6. Theodorsen, T., and Garrick, I. E.: General Potential Theory of Arbitrary Wing Sections. NACA Rep. No. 452, 1933.

TABLE I

SUMMARY OF VELOCITY-VECTOR DIAGRAM DATA FOR CONDITIONS A, B, AND C

	Condition A			Condition B			Condition C		
	Root	Mean	Tip	Root	Mean	Tip	Root	Mean	Tip
Axial velocity at survey station 2, V_{ax_2}, ft/sec	103.5	110.1	118.5	134.7	136.8	142.8	155.2	159.9	165.3
Velocity relative to casing at station 2, V_2, ft/sec	135.3	135.8	135.2	177.1	170.0	163.1	205.0	198.2	190.7
Velocity relative to rotor at station 2, W_2, ft/sec	384.9	419.9	449.1	421.2	447.5	467.6	445.9	470.4	490.4
Section angle of attack based on entering air vector, α_2, deg	9.3	8.1	6.5	6.2	5.5	4.0	4.5	3.4	2.1
Stagger angle based on entering air vector, β_2, deg	74.4	74.8	74.7	71.3	72.2	72.2	69.6	70.1	70.3
Mean air velocity relative to rotor, W_m, ft/sec	374.7	397.4	436.6	358.9	400.3	426.8	397.4	432.4	455.2
Section angle of attack based on mean air vector, α_m, deg	12.1	6.3	4.5	4.5	3.0	2.1	2.7	1.6	0.6
Stagger angle based on mean air vector, β_m, deg	77.2	73.0	72.7	69.7	69.7	70.3	67.8	68.3	68.8
Axial velocity at survey station 3, V_{ax_3}, ft/sec	62.3	121.9	141.2	114.0	141.2	145.4	145.0	160.1	164.7
Velocity relative to casing at station 3, V_3, ft/sec	98.2	125.6	145.6	114.4	141.2	145.6	148.9	164.1	166.0
Velocity relative to rotor at station 3, W_3, ft/sec	366.0	376.3	427.2	296.9	354.0	387.0	349.3	395.0	420.5
Effective turning angle, ϕ, deg	0.4	2.1	1.2	7.1	5.1	4.0	5.6	4.0	3.4

TABLE I - Concluded

SUMMARY OF VELOCITY VECTOR DIAGRAM DATA FOR CONDITIONS A, B, AND C - Concluded

	Condition A			Condition B			Condition C		
	Root	Mean	Tip	Root	Mean	Tip	Root	Mean	Tip
Change in tangential velocity of rotor, Δw, ft/sec	11.2	49.2	29.6	125.0	101.7	86.7	100.3	81.3	74.6
Change in tangential velocity of stator, Δw, ft/sec	87.1	79.4	65.1	115.0	100.9	78.8	134.0	117.1	95.1
Rotor speed, U, ft/sec	284.1	325.3	366.5	284.1	325.3	366.5	284.1	325.3	366.5
Section radius, r, ft	1.29	1.48	1.67	1.29	1.48	1.67	1.29	1.48	1.67

NATIONAL ADVISORY COMMITTEE FOR AERONAUTICS

TABLE II

SUMMARY OF COMPRESSOR DATA FOR CONDITIONS A, B, AND C

	Condition A	Condition B	Condition C
Weight flow $\frac{mg\sqrt{\theta}}{\delta}$, lb/sec	40.4	50.7	56.6
Volume flow at station 1, Q_1, cu ft/sec	545	683	757
Inlet density, ρ_1, slugs/cu ft	0.002252	0.002270	0.002305
Inlet stream static pressure, $p_1 - p_a$, lb/sq ft	-14.1	-21.9	-27.8
Midstage stream static pressure, $p_2 - p_a$, lb/sq ft	-20.8	-32.8	-45.5
Outlet stream static pressure, $p_3 - p_a$, lb/sq ft	53.7	47.0	25.0
Stage static-pressure rise from survey, Δp, lb/sq ft	67.8	68.9	42.8
Stage total-pressure rise from survey, ΔP, lb/sq ft	72.0	70.2	56.9
Total-pressure coefficient, C_P	2.120	1.993	1.547
Torque coefficient, C_T	0.146	0.162	0.155
Total-pressure efficiency, η	0.837	0.896	0.810
Mean stream static pressure, $p_m - p_a$, lb/sq ft	16.5	7.1	-10.3
Mean dynamic pressure, q_m, lb/sq ft	179.9	183.4	216.8
Mean section normal-force coefficient, c_n	0.548	0.552	0.438
Mean section lift coefficient, c_l	0.544	0.551	0.438
Mean air Mach number, M	0.346	0.350	0.382
Mean air Reynolds number, R_N	773,700	787,500	875,000

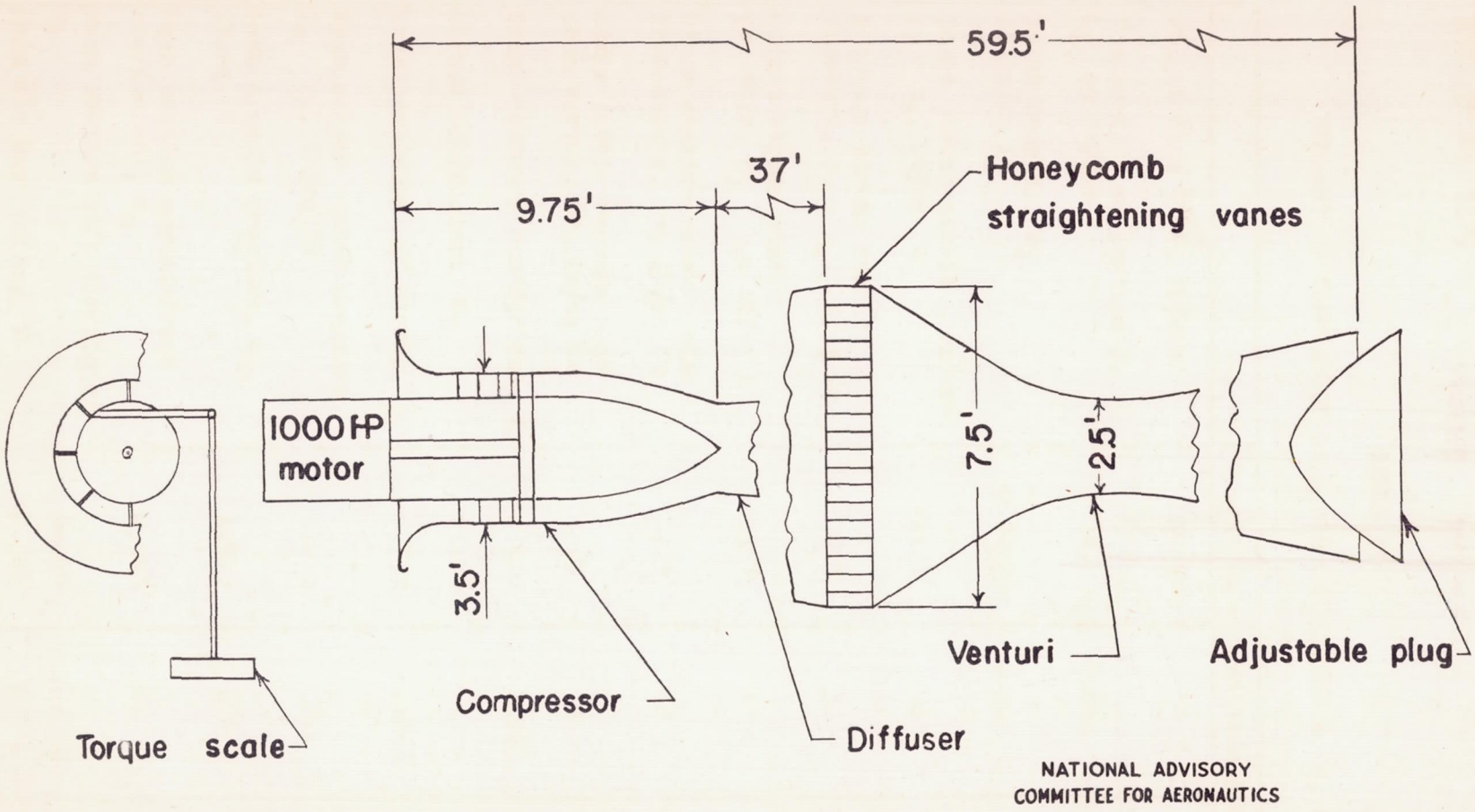

Figure 1. —— Schematic sketch of test arrangement.

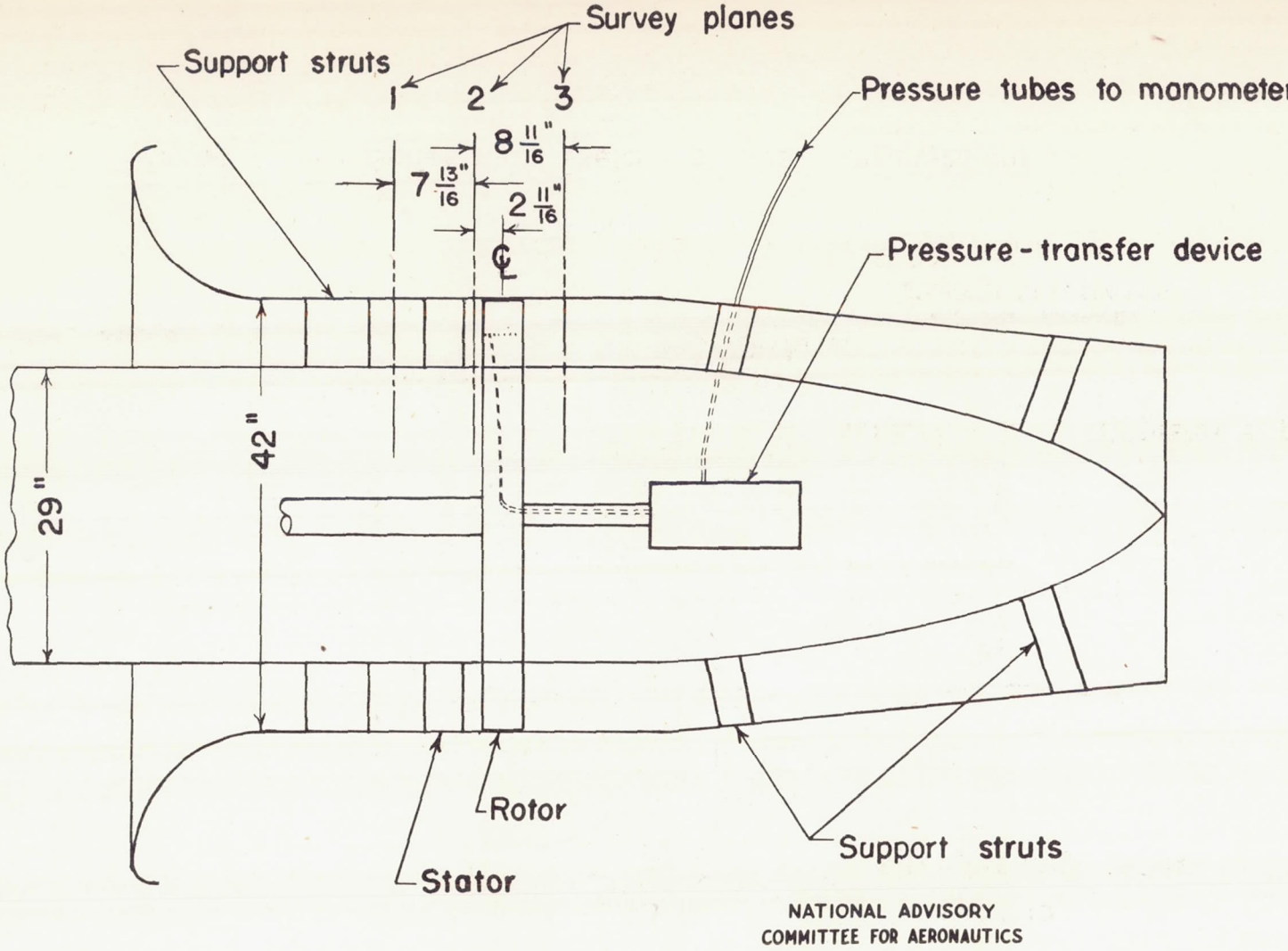

Figure 2. — Schematic sketch of compressor.

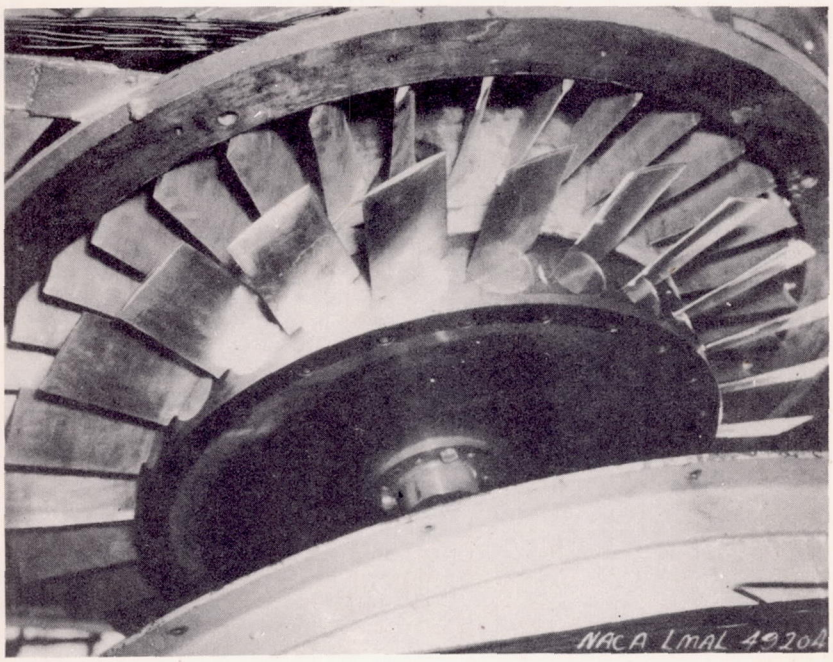

Figure 3.- Rear view of compressor with inner and outer casing removed.

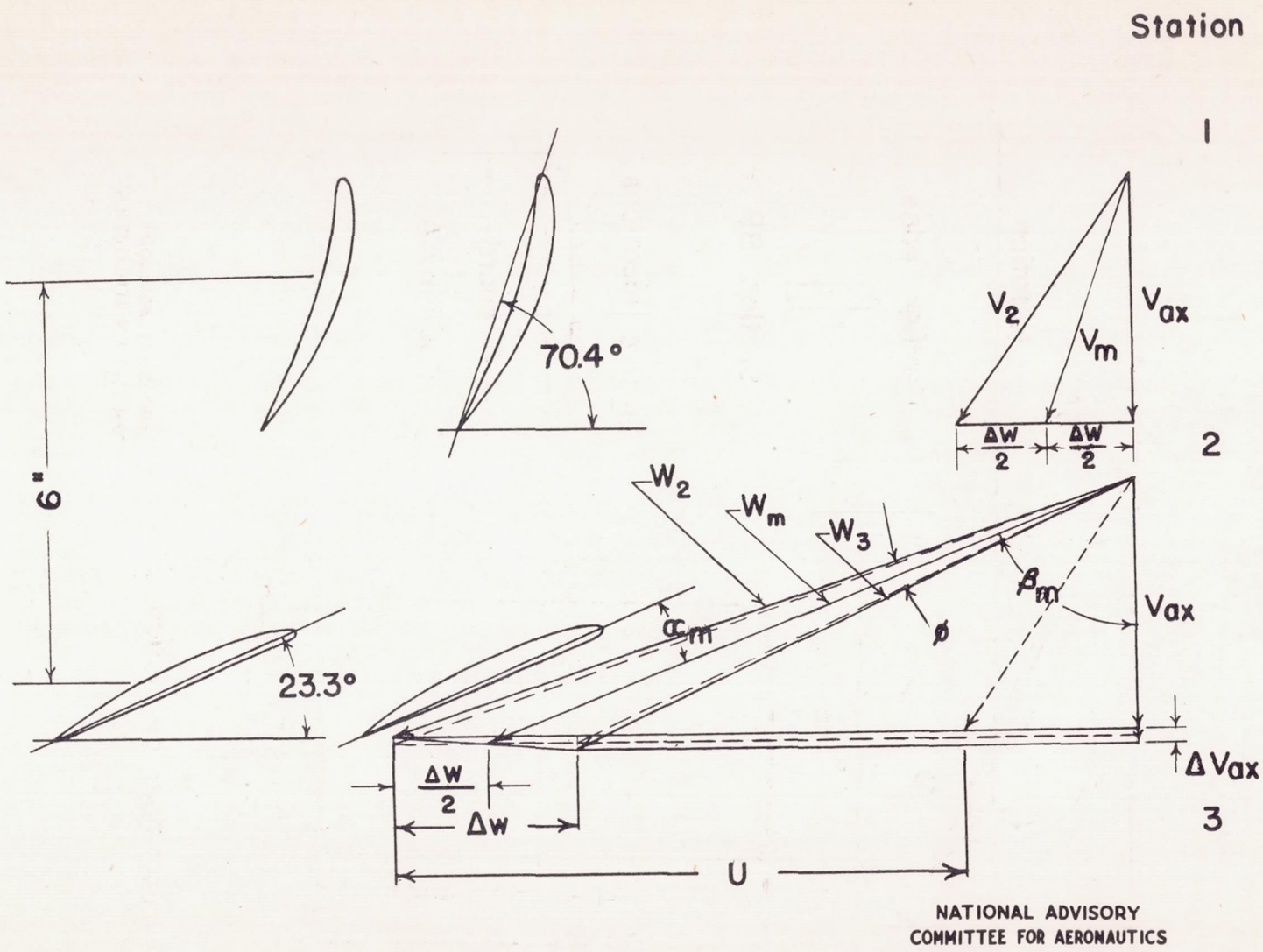

Figure 4. —— Typical velocity diagram for stator and rotor, mean radius section.

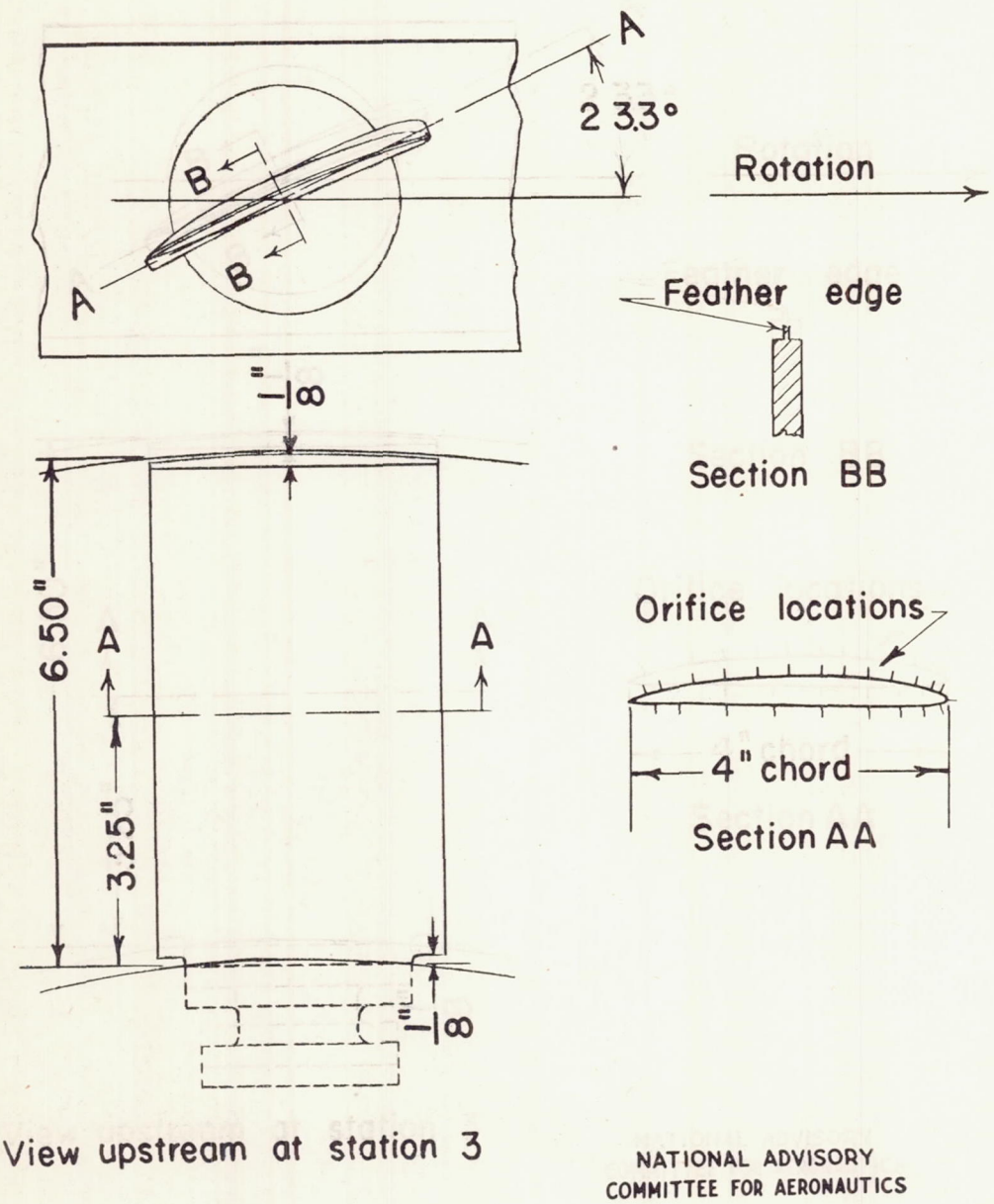

Figure 5 .— Sketch of rotor blade showing orifice locations.

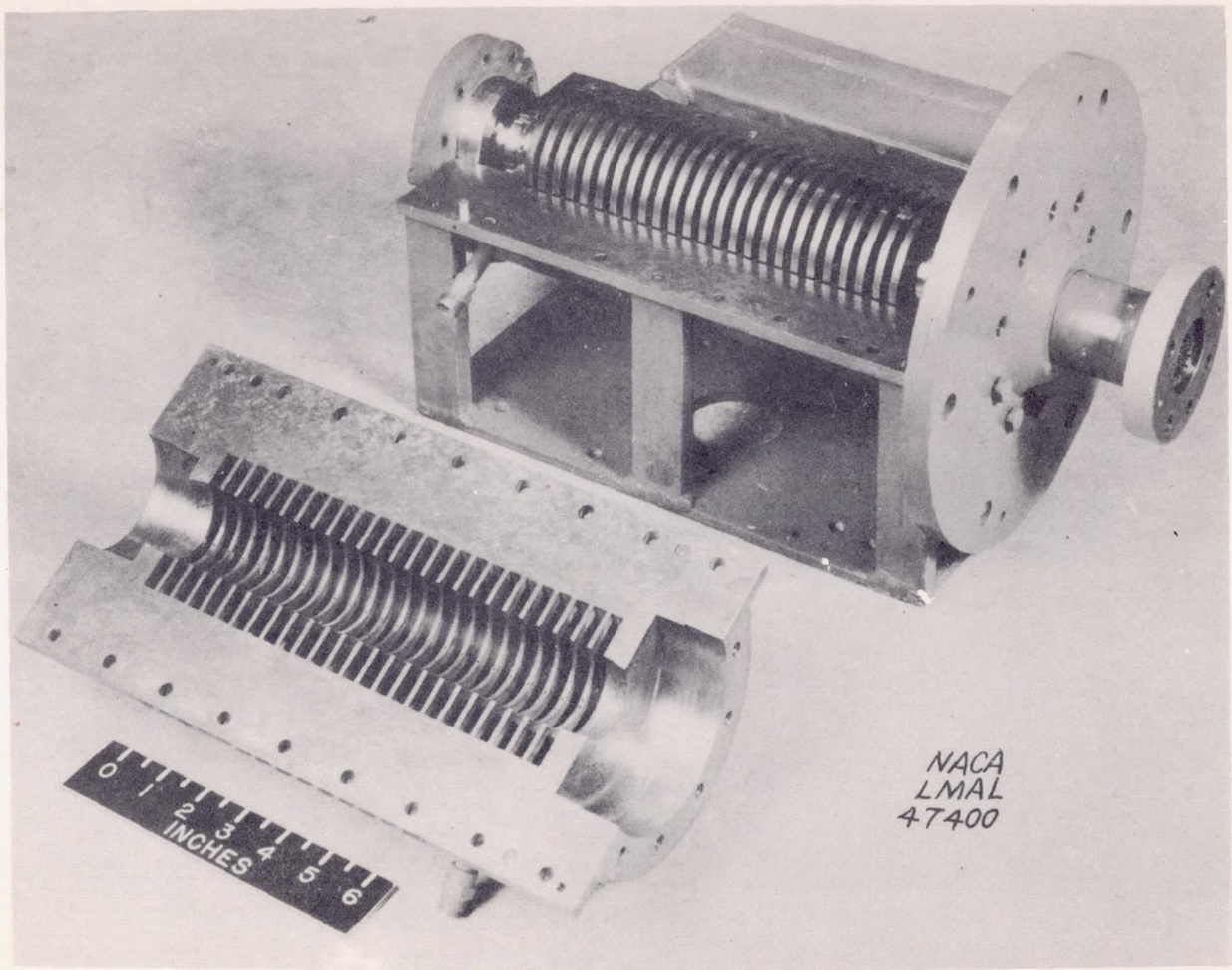

Figure 6.- Pressure-transfer device with top half of casing removed.

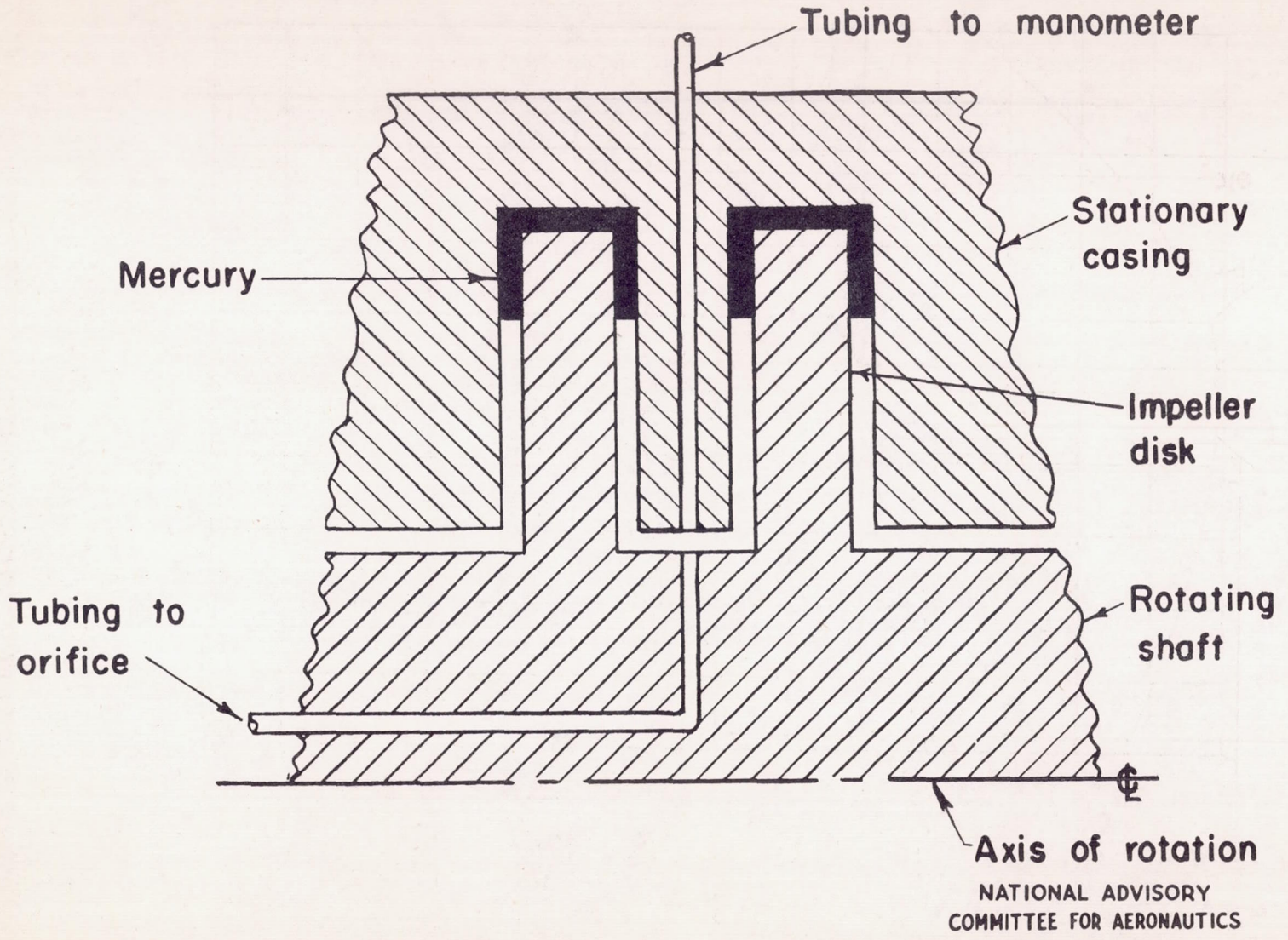

Figure 7. — Schematic diagram of pressure-transfer element.

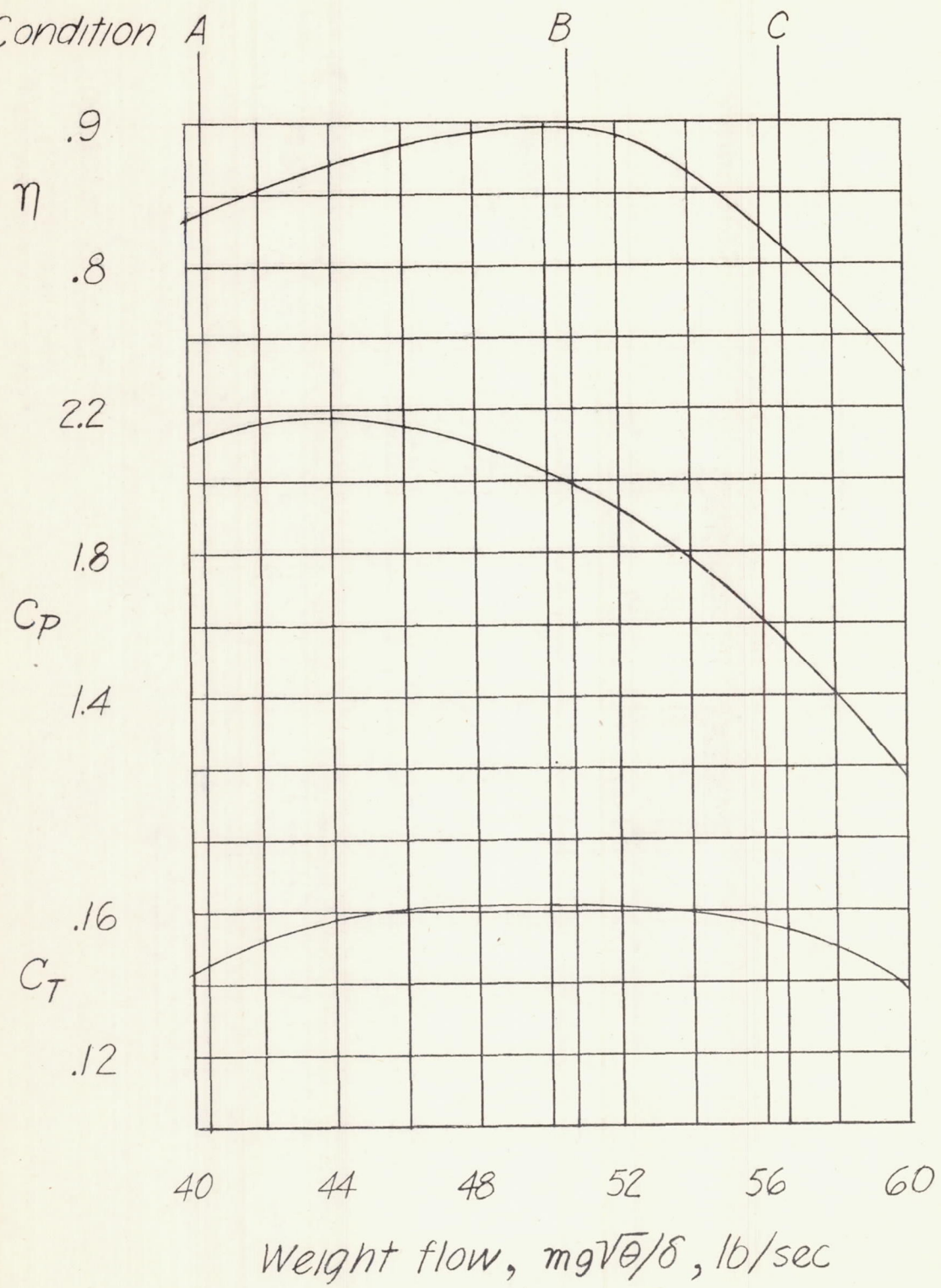

Figure 8.-Performance curves for compressor. Rotor speed, 2100 rpm.

NATIONAL ADVISORY
COMMITTEE FOR AERONAUTICS

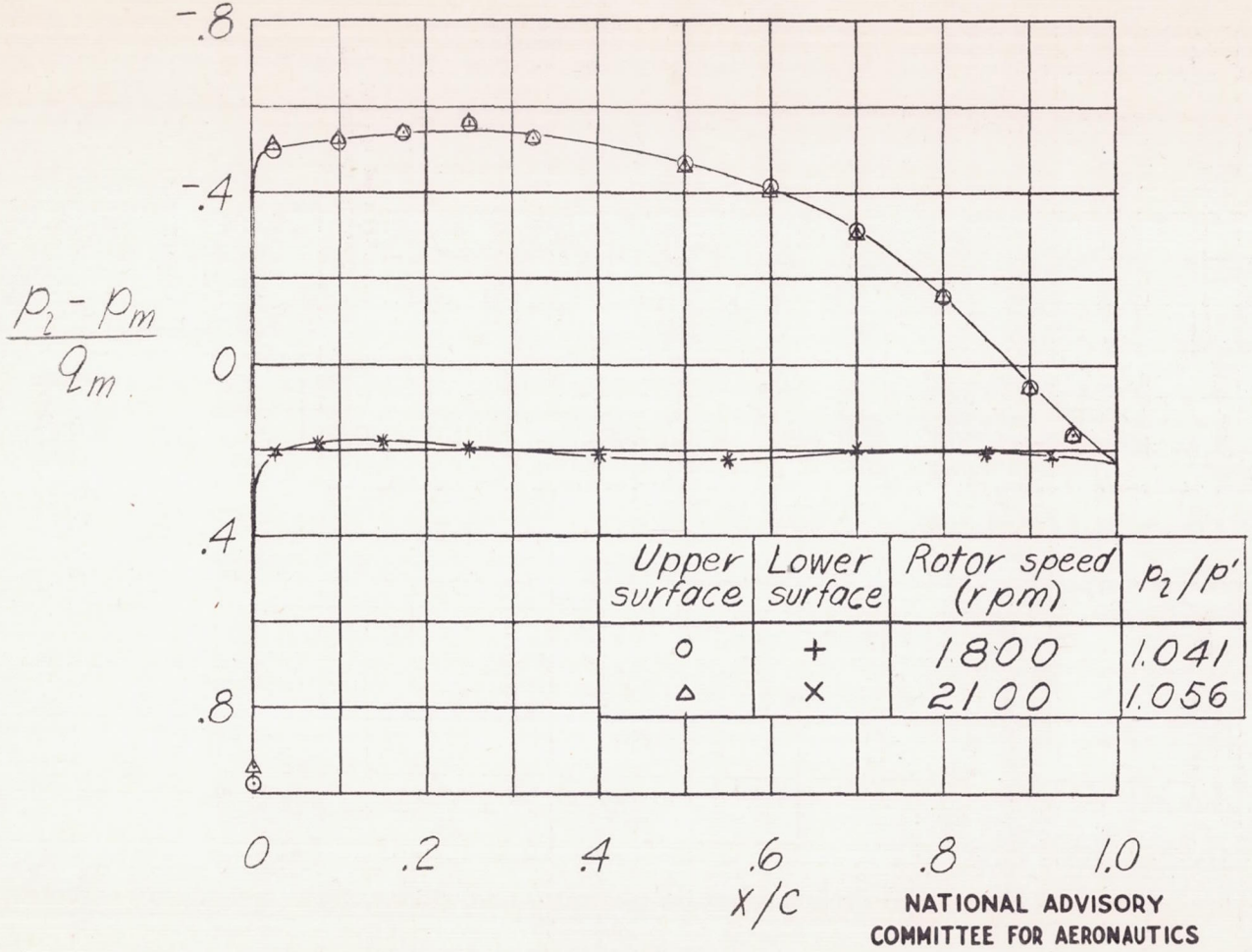

Figure 9.- Comparison of pressure coefficients for two rotational speeds. $\alpha_m = 3.0°$, $C_l = 0.55$.

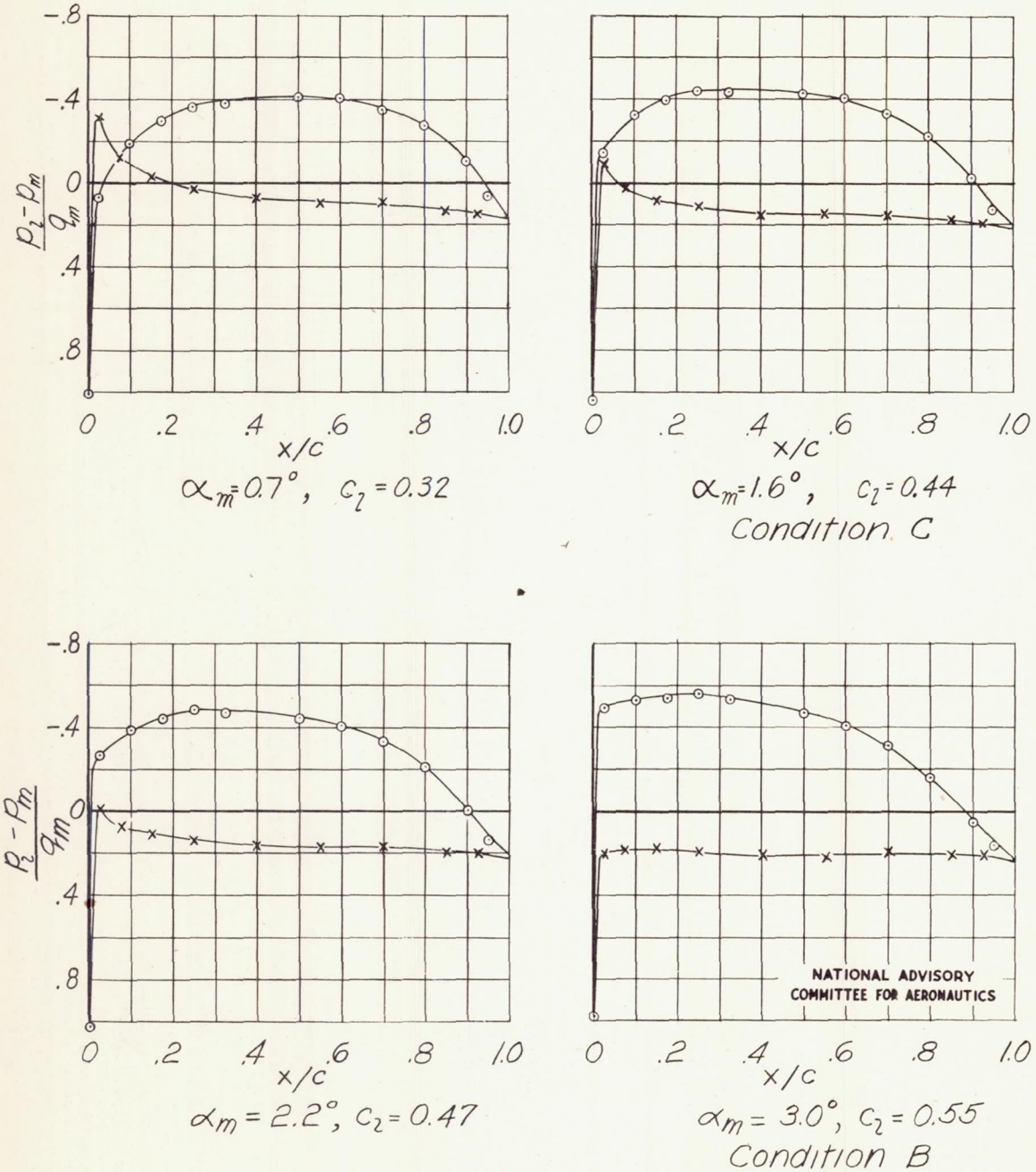

Figure 10.- Pressure distributions on rotor blade. Rotor speed, 2100 rpm.

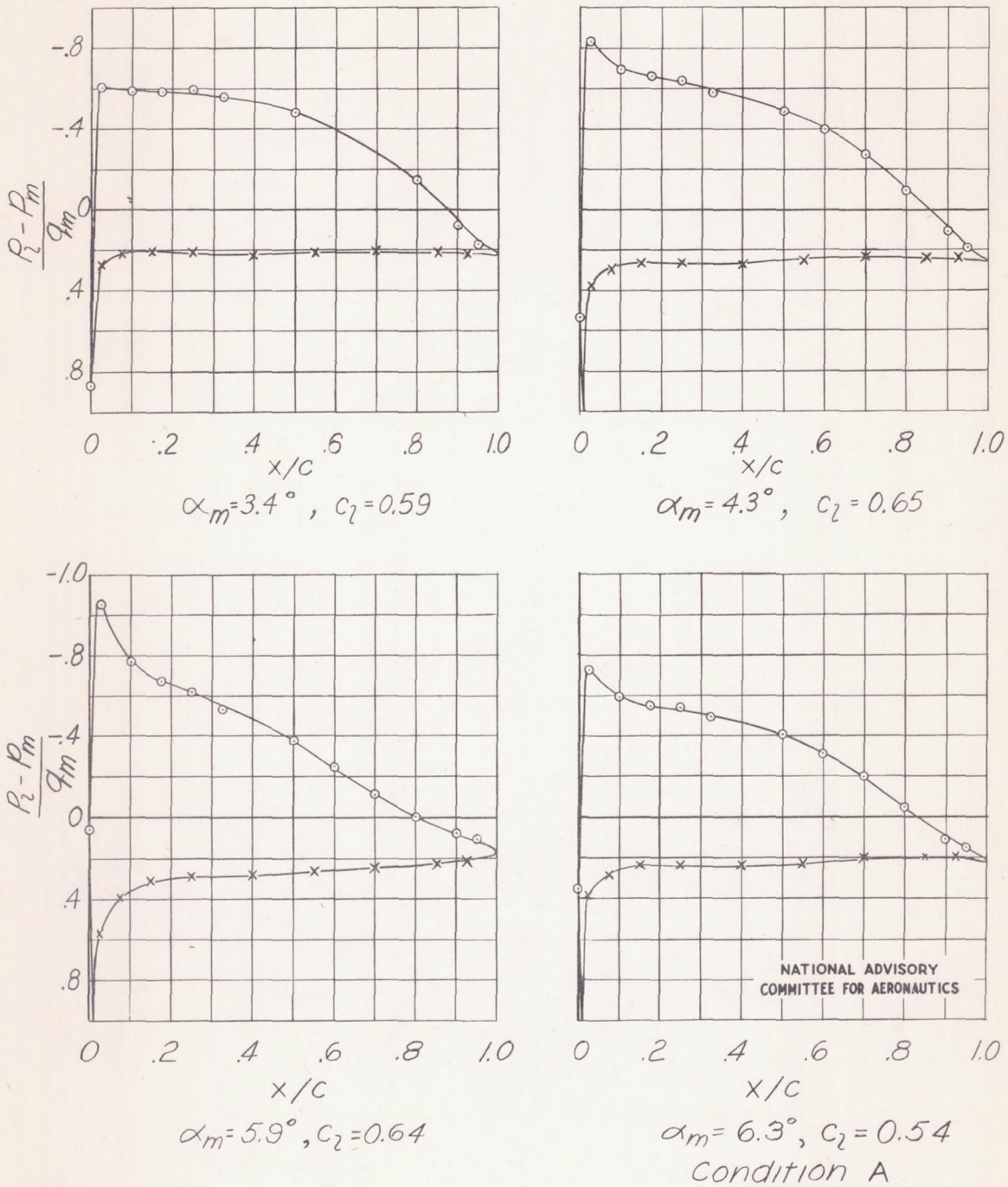

Figure 10.- Concluded.

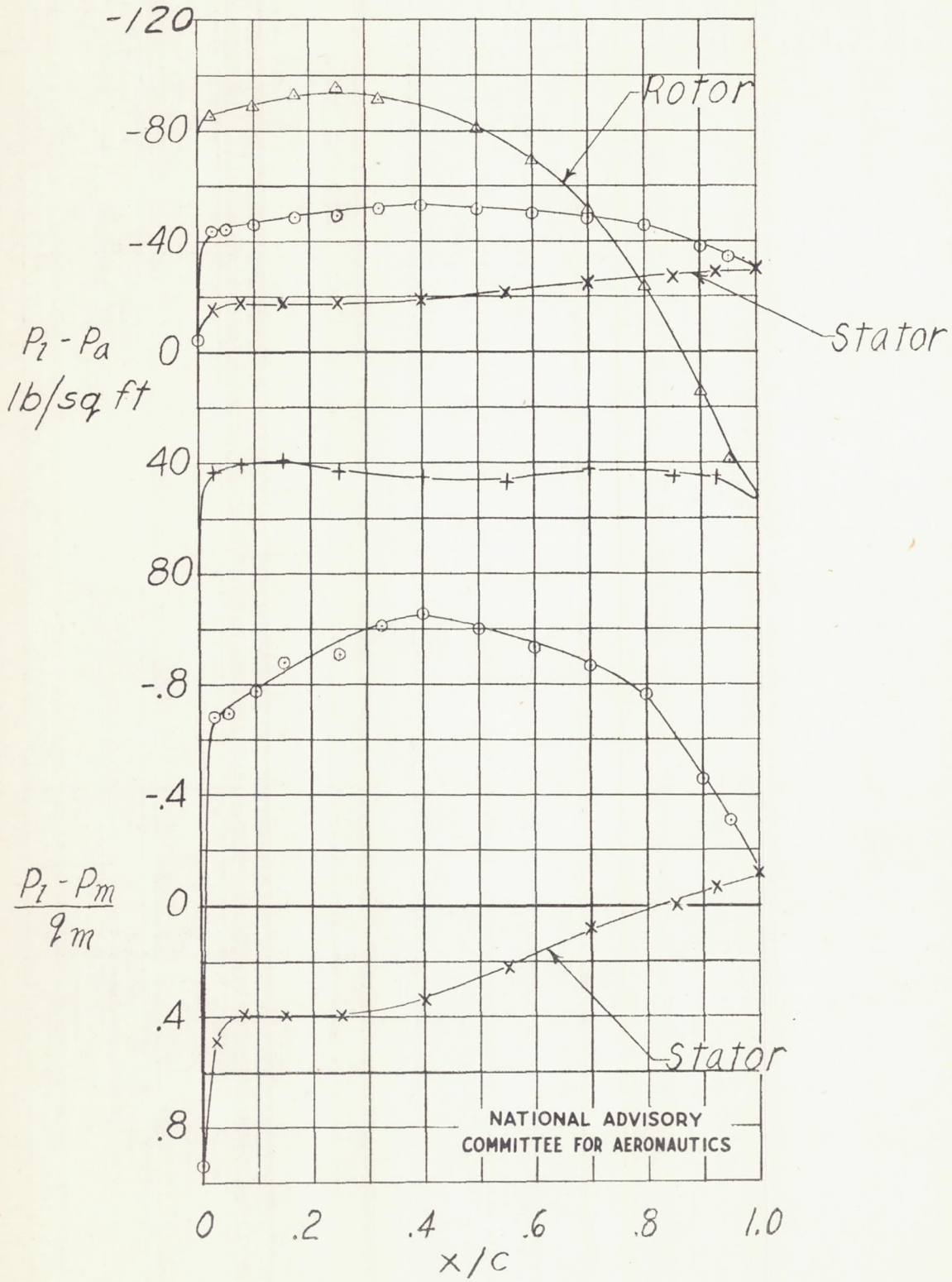

Figure 11.- Comparison of rotor and stator pressures.

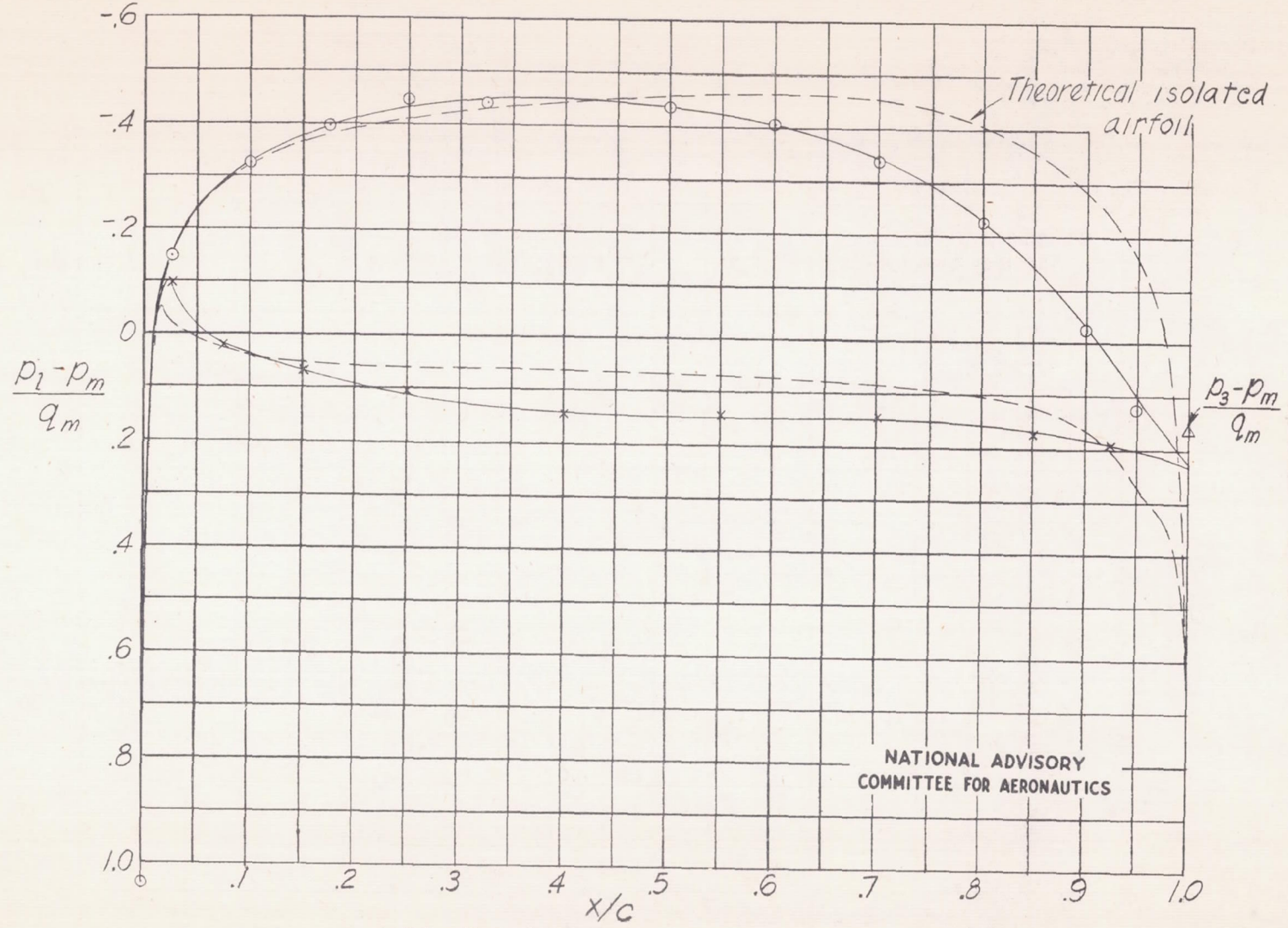

(a) Condition C, $c_l = 0.44$.

Figure 12.- Comparison of theoretical and experimental pressure distributions.

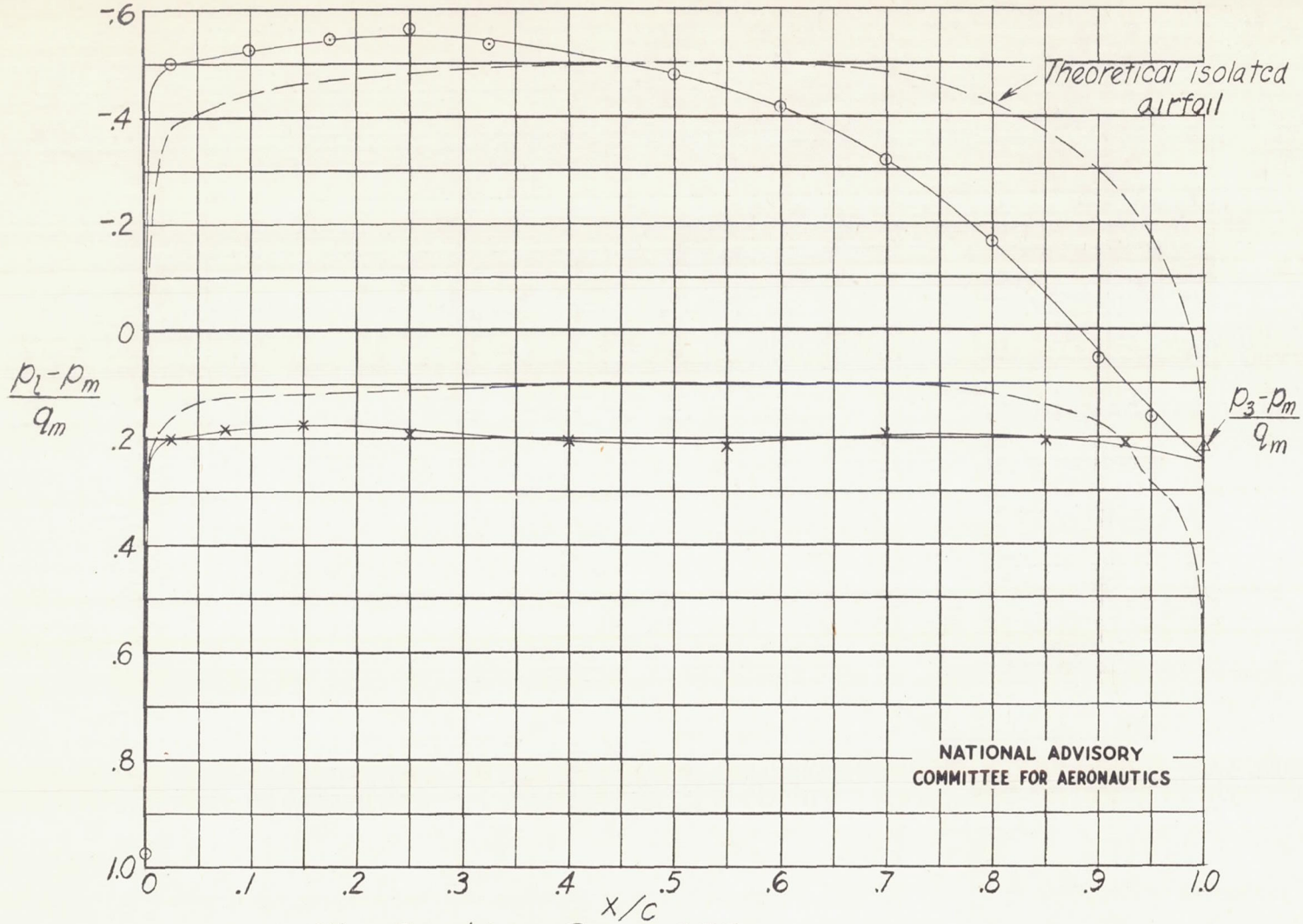

(b) Condition B, $c_l = 0.55$.

Figure 12.- Concluded.

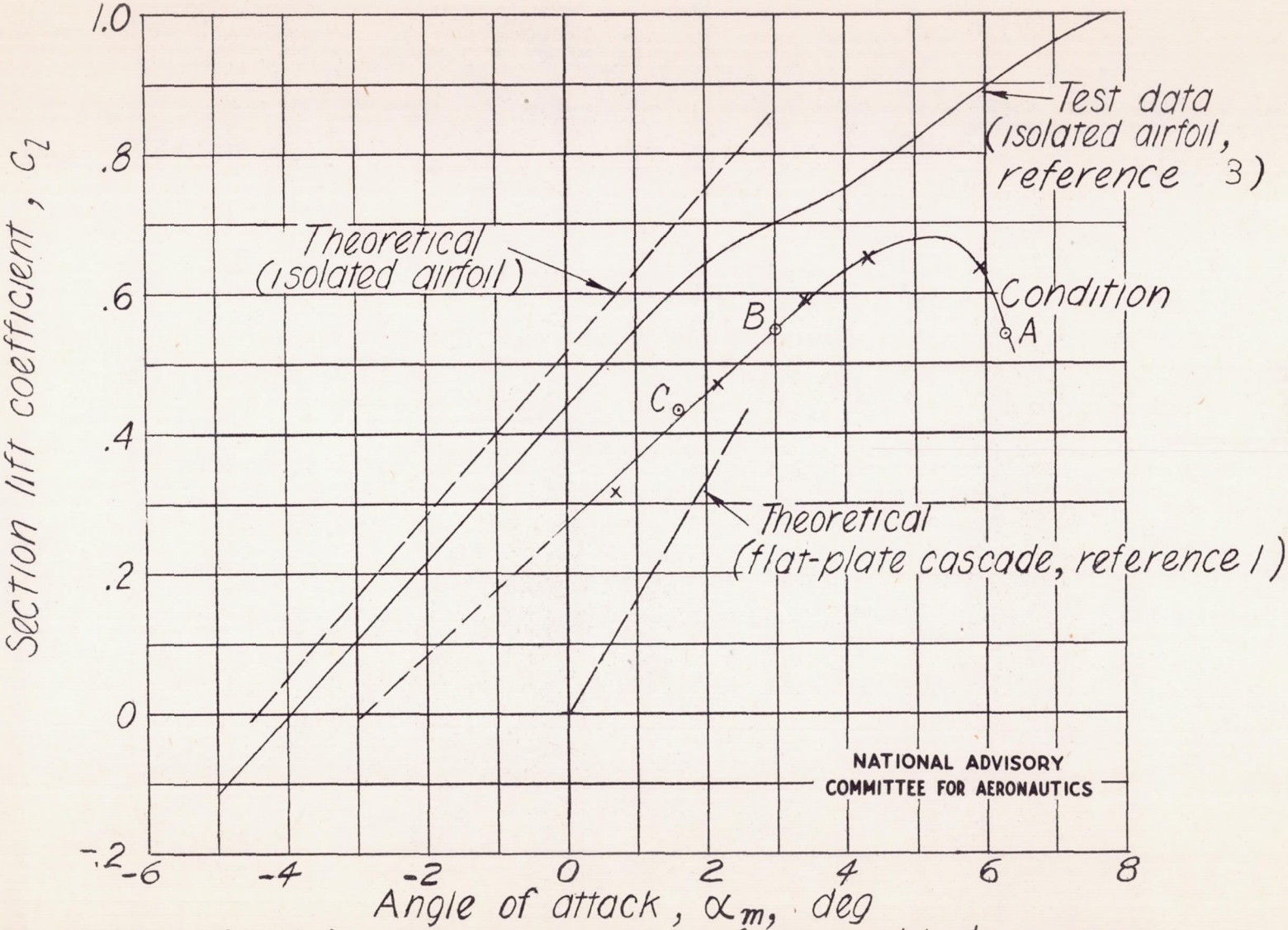

Figure 13.- Lift characteristics of rotor blade section.